



Programming curvilinear paths of flat inflatables

Emmanuel Siéfert, Etienne Reyssat, José Bico, Benoît Roman

► To cite this version:

Emmanuel Siéfert, Etienne Reyssat, José Bico, Benoît Roman. Programming curvilinear paths of flat inflatables. Proceedings of the National Academy of Sciences of the United States of America, 2019, 116 (34), pp.16692-16696. 10.1073/pnas.1904544116 . hal-02298418

HAL Id: hal-02298418

<https://hal.sorbonne-universite.fr/hal-02298418>

Submitted on 26 Sep 2019

HAL is a multi-disciplinary open access archive for the deposit and dissemination of scientific research documents, whether they are published or not. The documents may come from teaching and research institutions in France or abroad, or from public or private research centers.

L'archive ouverte pluridisciplinaire **HAL**, est destinée au dépôt et à la diffusion de documents scientifiques de niveau recherche, publiés ou non, émanant des établissements d'enseignement et de recherche français ou étrangers, des laboratoires publics ou privés.

Programming curvilinear paths of flat inflatables

Emmanuel Siéfert^a, Etienne Reyssat^a, José Bico^a, and Benoit Roman^a

^aLaboratoire de Physique et Mécanique des Milieux Hétérogènes, CNRS, ESPCI Paris, PSL Research University, 7 quai Saint Bernard, 75005 Paris, France, and Sorbonne Universités, Université Paris Diderot

This manuscript was compiled on September 7, 2019

Inflatable structures offer a path for light deployable structures in medicine, architecture and aerospace. In this study, we address the challenge of programming the shape of thin sheets of high stretching modulus, cut and sealed along their edges. Internal pressure induces the inflation of the structure into a deployed shape that maximizes its volume. We focus on the shape and nonlinear mechanics of inflated rings and, more generally, of any sealed curvilinear path. We rationalize the stress state of the sheet and infer the counter-intuitive increase of curvature observed upon inflation. In addition to the change of curvature, wrinkles patterns are observed in the region under compression in agreement with our minimal model. We finally develop a simple numerical tool to solve the inverse problem of programming any two-dimensional curve upon inflation and illustrate the application potential by moving an object along an intricate target path with a simple pressure input.

Tension field theory | Wrinkling instability | Programmable structures

A new domain of application for pneumatic structures has emerged with the current development of soft robotics actuators (1). Uni-directional bending of elastomeric pneumatic structures can be easily controlled by internal pressure (2), and recently more general complex shape-morphing was achieved (3). As they rely on large material strains, these structures are based on elastomers, and therefore have a relatively low stiffness, which makes them unsuitable for large scale structures and heavy loads. In contrast, stiff inflatables may be obtained by stitching flat pieces of thin but nearly inextensible material. As a first example, sky lanterns were invented during the third century in China (4), then rediscovered and scaled up by the Montgolfier brothers for ballooning in the 18th century. Since then, stiff inflatables have been widely used in engineering(5), medicine (6), architecture and aerospace (7–9). Here, we show how to shape-program slender “flat-inflatable” structures which are extremely easy to manufacture : two identical patches are cut in thin sheets and sealed along their boundaries (10). Common examples from everyday life are Mylar balloons. Although they are easy to manufacture, predicting the 3D shape of such flat-inflatable structures, i.e. maximizing a volume that a thin inextensible sheet can encompass remains a challenge due to geometrical constraints. Indeed, changing the Gaussian curvature, i.e. the product of both principal curvatures of a surface, implies a distortion of the distances within the surface. In the case of thick elastic plates, local stretching or compression may accommodate changes in metrics. However, inextensible sheets behave nonlinearly: they can accommodate compression by forming wrinkles, but cannot be stretched. Tension field theory, the minimal mathematical framework to address this problem, has been developed to predict the general shape of initially flat structures. While solutions have been found for axisymmetric convex surfaces (11–13) and polyhedral structures (14, 15), predictions in a general case remain an open issue and have



Fig. 1. Flat sealed inflatables. (A) Heat sealing of two sheets together along a desired path using a soldering iron mounted on an XY-plotter. (B) Photograph of an experimental realization of inflating an annulus of inner radius R and width w , with $R/w \rightarrow 0$. Wrinkles appear and two diametrically opposed kinks are observed. (C) For $R/w \gg 1$ the inflated structure buckles smoothly out of plane. Both structures are made of Thermo-Plastic-polyUrethane coated nylon fabric.

been addressed numerically in the computer graphics community (16). In a seminal paper, G.I. Taylor described the shape of an axisymmetric parachute with an unstretchable sail (17), a solution also appearing in recent studies on the wrapping of

Significance Statement

Inflatable structures are flat and foldable when empty and both lightweight and stiff when pressurized and deployed. They are easy to manufacture by fusing two inextensible sheets together along a defined pattern of lines. However, the prediction of their deployed shape remains a mathematical challenge, which results from the coupling of geometrical constraints and the strongly non-linear and asymmetric mechanical properties of their composing material: thin sheets are very stiff upon extensional loads, while they easily shrink by buckling or wrinkling when compressed. We discuss the outline shape, local cross-section and state of stress of any curvilinear open path. We provide a reverse model to design any desired curved two-dimensional shape from initially flat tubes.

E.S. and B.R. developed the flat inflatables concept. E.S. designed and conducted the experiments. All authors contributed to the theoretical model and participated to the redaction of the manuscript.

The authors declare no conflict of interest

²To whom correspondence should be addressed. E-mail: emmanuel.siefert@espci.fr

droplets with thin polymeric sheets (18–20).

We study macroscopic structures made of thin quasi-inextensible planar sheets heat-sealed along a desired path using a soldering iron with controllable temperature mounted on the tracing head of an XY-plotter (10) (Fig. 1A, see Materials and Methods). We focus on simple configurations where pairs of identical flat patches forming curvilinear paths of constant width are bonded along their edges. When inflating a straight ribbon, we trivially obtain, far from the extremities, a perfect cylinder of circular cross-section. In contrast, inflating a flat ring results into complex features. We observe for instance an out-of-plane instability in the case of closed paths and the presence of radial wrinkles and folds (Fig. 1B,C). We show in this article that inflation induces an over-curvature of the outline, through a detailed study of its cross-section. We first describe the cross-section of axisymmetric annuli. We then extend our analysis to open rings to predict the position of compressive zones and the change in intrinsic curvature. We finally devise an inverse method for programming the outline of any arbitrary inflated curved flat path and illustrate the strong workload capacity of these actuators by displacing an object along a complex path with a simple pressure input.

Results and Discussion

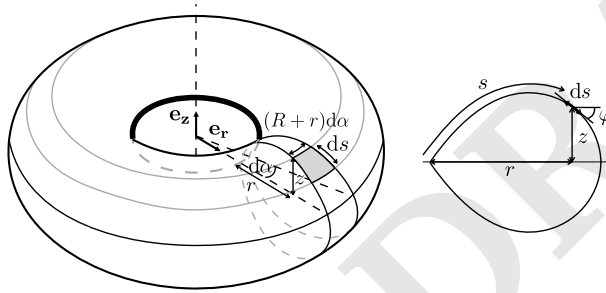


Fig. 2. Sketch of the inflated ring with the definition of the parameters and coordinates, where $R + r$ is the radial distance to the axis of symmetry, z the height, s the curvilinear coordinate along the membrane in the $(\mathbf{e}_r, \mathbf{e}_z)$ plane, and $\tan \varphi$ the local slope of the profile.

Closed rings. We first consider a swim ring configuration: a planar axisymmetric annulus of inner radius R and width w . We describe the cross section of the inflated annulus in the $(\mathbf{e}_r, \mathbf{e}_z)$ plane as $[R + r(s), z(s)]$ with the curvilinear abscissa $s \in [0, w]$ (Fig. 2). We assume that the structure is in a doubly-asymptotic regime: the sheet may be considered as inextensible (i.e. $p \ll Et/w$) but can accommodate any compression by forming wrinkles or folds (21–24) ($p \gg Et^3/w^3$). The shape of the membrane may therefore be obtained by maximizing the enclosed volume (see Supplementary Information). Here we choose to derive this shape by considering the balance of tension along the membrane path and applied pressure in the r - z plane. Owing to inextensibility, the hoop direction conversely undergoes contraction, except along the inner perimeter of the torus. Indeed, all material points have a radial displacement component towards the axis of symmetry of the torus when

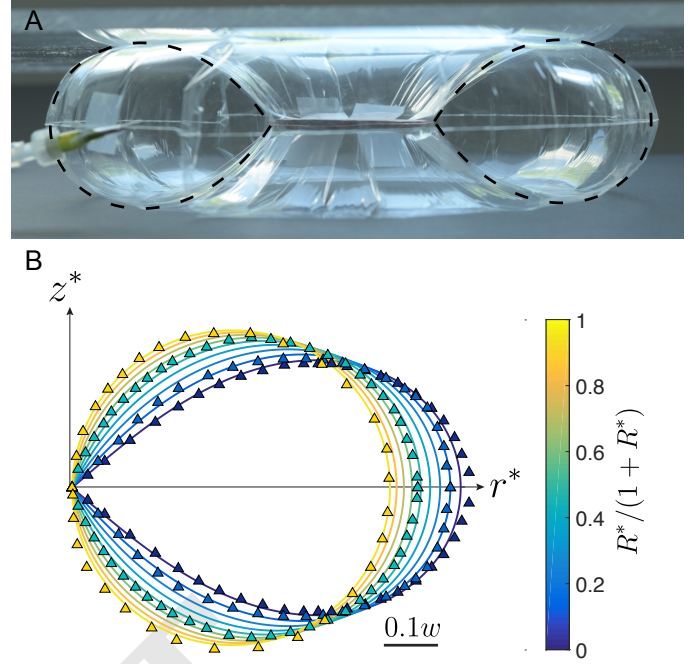


Fig. 3. Cross-section of a closed inflated annulus. (A) Profile picture of a closed inflated annulus, the axisymmetry of the structure being constrained by two plates to prevent out-of plane buckling. The ring is made of a 16 μm thick polypropylene sheet of inner radius $R = 25$ mm and outer radius $R + w = 130$ mm. Dashed lines correspond to the theoretical cross sections.

Note that the wrinkles extend through the whole torus. (B) Theoretical (solid lines) and experimental (triangles) rescaled cross sections of inflated closed rings for various aspect ratios $R^*/(1 + R^*)$ with $R^* = R/w$. $r^* = r/w$ and $z^* = z/w$ correspond to the rescaled radial and vertical coordinates, respectively.

inflated. Following the framework proposed by G.I. Taylor (17), we define a tension per unit length T (defined in the inflated state, as in Fig.2 and Supplementary Fig.S1) and we consider the force balance along a surface element of extent ds on an angular section $d\alpha$ (Fig. 2). In the absence of forces in the compressed hoop direction, balancing the force in the tangent plane of the surface element reads $d((R + r)T)/ds = 0$. The tension thus reads $T = C/(R + r)$, where C is a constant to be determined. The tension along the curved membrane balances the pressure force acting normal to the surface element following Laplace law and reads:

$$\frac{d\varphi}{ds} = -\frac{p}{C}(R + r) \quad [1]$$

where $\tan \varphi$ is the slope of the cross section with respect to \mathbf{e}_r . Using the geometrical relation $\cos \varphi = dr/ds$, differentiating [1] shows that the shape of the section is the solution of the classical non-linear oscillator ODE for $\varphi(s)$:

$$\frac{d^2\varphi}{ds^2} = -\frac{p}{C} \cos \varphi, \quad [2]$$

which must be complemented by boundary conditions. Symmetry with respect to the plane $z = 0$ imposes $z(0) = z(w) = 0$, which leads to the boundary condition $\int_0^w \sin \varphi ds = 0$ for equation 2. A second imposed condition is that the inner seam

remains under tension, which leads to $r(0) = 0$. The force balance normal to the surface of the sheet (equation 1) provides the corresponding condition for φ : $d\varphi/ds(0) = -Rp/C$. The absence of radial force at the outer seam imposes $\varphi(w) = -\pi/2$. A detailed justification of these boundary conditions and of Eqs. 1, 2 may be found in Supplementary, using variational techniques. The equation is solved with standard shooting methods, which determines the constant p/C . Using $\cos \varphi = dr/ds$ and $\sin \varphi = dz/ds$, we translate the solution $\varphi(s)$ into the corresponding $z(r)$ profile. Denoting dimensionless lengths with the subscript $*$, we display the dimensionless shapes $z^* = z/w$ vs. $r^* = r/w$ in Fig. 3B (solid lines) and compare them with experimental profiles (triangles in Fig. 3B and image in Fig. 3A) for values of the aspect ratio $R^*/(1+R^*) = R/(w+R)$ ranging from 0.05 to 0.95. For slender geometries, *i.e.* $R^* = R/w \gg 1$, the section of the torus is a circle, as expected for a straight elongated balloon. For smaller values of R^* , the section presents a singular wedge along the inner radius of the torus (Fig. 3A-B and Supplementary information). The agreement between calculated and measured profiles is remarkable without any adjustable parameter. The toroidal structure is, as predicted by the geometrical model, decorated with alternating wrinkles and crumples (21, 25), everywhere except at the inner edge of the structure (Fig. 3A and Supplementary Fig. S2). However, we observe that the global structure does not remain in-plane upon inflation and tends to buckle out of plane, exhibiting either diametrically opposed localized kinks for very thin sheets and $R^* \sim 1$, or a regular oscillating shape for relatively thicker sheets, $R^* > 1$ and high enough pressures (see Fig. 1, Supplementary Movie 1, Supplementary Fig. S2).

Coiling of open rings. These observations suggest the existence of geometrical frustration in closed inflated rings, which is reminiscent of the buckling of rings with incompatible intrinsic curvature (26), or of the warping of curved folds (27). This constraint is readily assessed when a cut is performed on the annuli (and both ends sealed), thus removing the closing condition. With this additional degree of freedom, the structures remain in-plane, but the curvature of their outline increases, which results into an overlapping angle $\Delta\alpha$ (Fig. 4A). Considering a cut in the $(\mathbf{e}_r, \mathbf{e}_z)$ plane, the pressure force acting on one half of the ring is $2pA$ where $2A$ is the area of the two cross sections. In the closed configurations, the membrane tension balancing this separating pressure force is entirely supported by the inner seam, all other points of the membrane being under hoop compression. On a single cross section, the pressure force induces a residual torque with respect to the inner seam. For an open ring, having a free end and no external loading imposes a vanishing internal torque in any cross section of the structure. The initially unbalanced pressure torque induces the curvature of the structure until two symmetric lines of tension appear and provide internal torque balance (Fig. 4D). Counter-intuitively, pressurizing curved structures increases their curvature.

We show in the Supplementary Information that overcoiling is associated with an increase of the enclosed volume and assume that the optimal coiling is determined by the inextensibility condition. For a quantitative description, we consider an open annulus of inner radius R and width w in the flat configuration. The overlap results into a new inner radius $R_1 = R/(1 + \epsilon_\alpha)$, with the strain $\epsilon_\alpha = \Delta\alpha/2\pi$. we

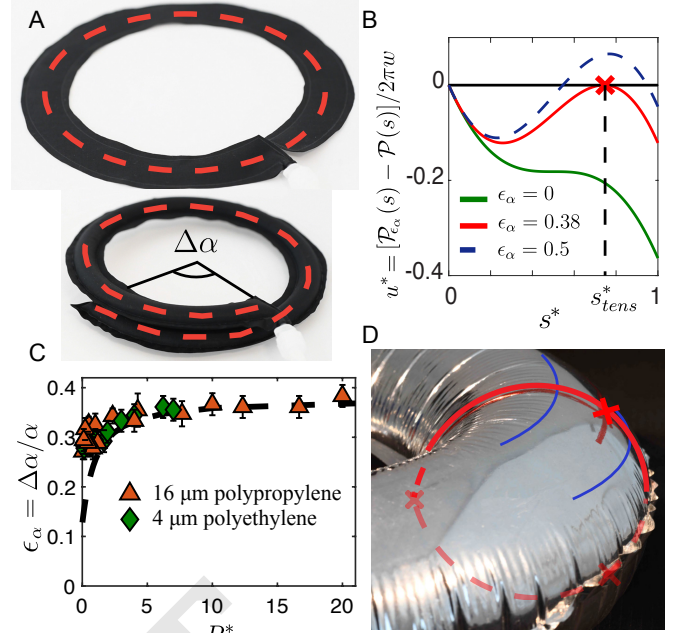


Fig. 4. Overcurvature of an open torus. (A) A circular annulus cut and sealed (upper image) curves more upon inflation (lower image) and exhibits an excess angle $\Delta\alpha$. (B) Dimensionless perimeter difference u^* as a function of the curvilinear coordinate s^* for various overcurvature strains ϵ_α , in the case $R \gg w$ (circular section upon inflation). $u^* = 0$ in the flat state; green line, upon inflation with $\epsilon_\alpha = 0$; red line, for $\Delta\alpha_{tens} \simeq 137^\circ$ (the red cross indicates the abscissa s^*_{tens} under tension); dashed blue line, for $\epsilon_\alpha = 0.5$ (this solution is not physically relevant since it implies azimuthal extension). (C) Experimental and theoretical (dashed line) target curvature change as a function of the ratio R/w . Triangles: experiments with $16\mu\text{m}$ thin sheets of polypropylene; diamonds: experiments with $4\mu\text{m}$ thin sheets of polyethylene. (D) Wrinkles are absent along a band of finite width, highlighted in blue. The red line corresponds to the theoretically calculated profile (within the limit of inextensibility) and the red crosses mark the positions of the tensions lines for $R/w = 3$.

assume that, far from the ends of the open annuli, the family of profiles calculated for closed rings remains valid. However, the current shape profile $r_1(s)$ corresponds to the new aspect ratio $R_1^* = R_1/w$. The local projected perimeter of the structure at the curvilinear coordinate s is thus equal to $\mathcal{P}_{\epsilon_\alpha}(s) = 2\pi(1 + \epsilon_\alpha)[R_1 + r_1(s)]$. Due to inextensibility condition, this perimeter is bounded by its initial value in the flat configuration $\mathcal{P}(s) = 2\pi(R + s)$. We represent in Fig. 3B the normalized difference

$$u^* = [\mathcal{P}_{\epsilon_\alpha}(s) - \mathcal{P}(s)] / 2\pi w = (1 + \epsilon_\alpha)r_1^*(s^*) - s^* \quad [3]$$

as a function of the non-dimensional abscissa s^* , imposing ϵ_α for the case of $R^* \gg 1$. As described previously, u^* is always negative for $\epsilon_\alpha = 0$, that is, all material points are under azimuthal compression except for the inner point $s^* = 0$ (Fig. 3B). As ϵ_α is increased, the curve $u^*(s^*)$ presents a secondary maximum which increases. This maximum eventually reaches 0 at a position s^*_{tens} for a particular value ϵ_α^{tens} (Fig. 3B). Beyond this point, u^* is partly positive, which breaks the inextensibility condition. As the open structure is inflated, we thus expect ϵ_α to take the value ϵ_α^{tens} , for which mechanical equilibrium is attained with two additional up-down symmetric lines of tension along the membrane. Although in Eq. (3) the profile $r_1(s^*)$ depends, in principle, on ϵ_α , we assume here that this dependence remains modest.

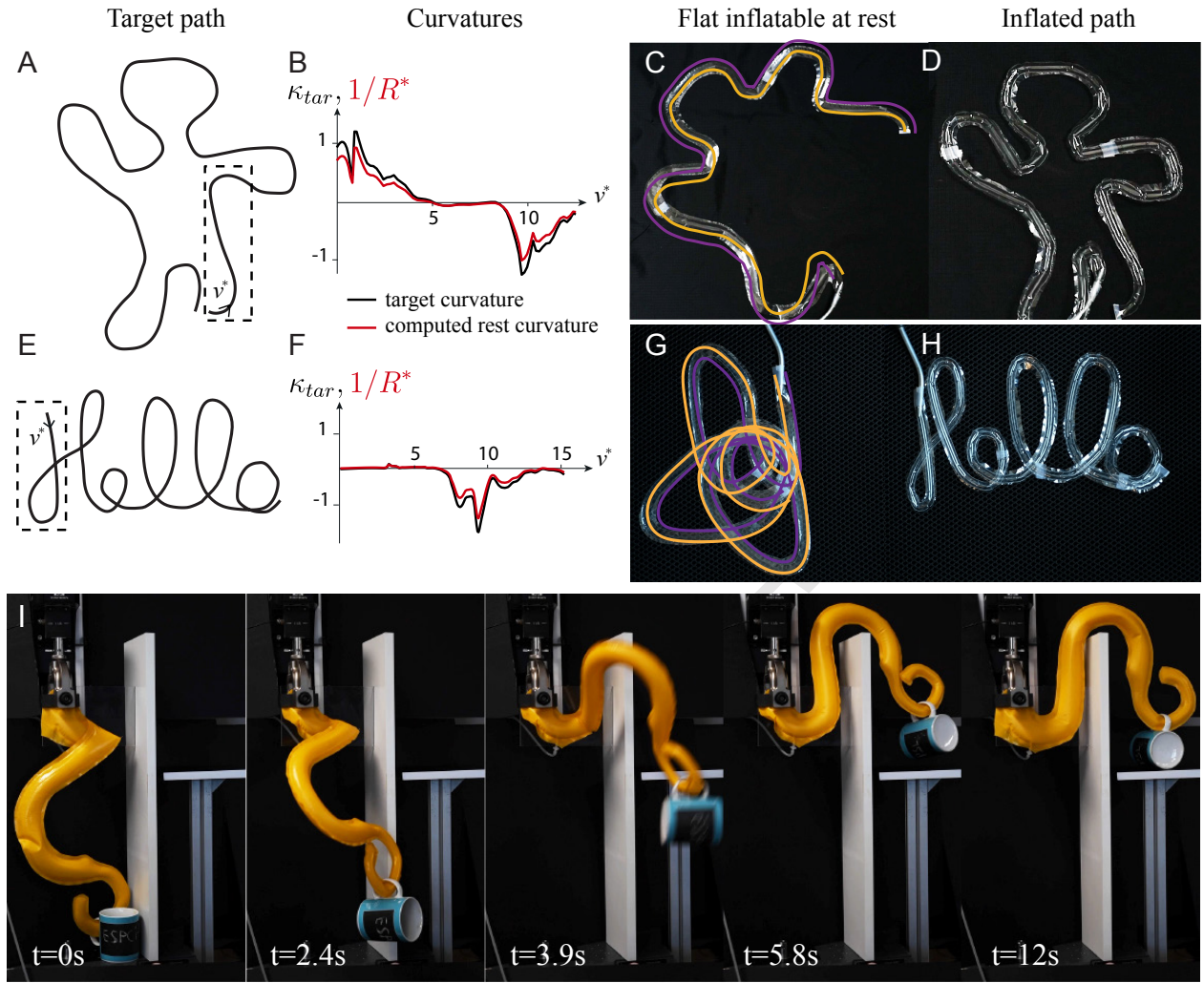


Fig. 5. Inverse problem for getting any curved shape. (A) and (E), target path; (B) and (F), normalized target and rest curvature, for a given path width w , κ_{tar} and $1/R^*$ as a function of the curvilinear coordinate $v^* = v/w$ of a portion of the target path, highlighted in (A) by a dashed box. The curvature of the flat path is computed using the prediction for curvature change plotted in Fig. 3C, that is according to equation [4]. (C) and (G), flat path computed by the inverse model on top of a photograph of the experimental realization. (D) and (H), same path under pressure, fitting closely the target curve (see supplementary Video 3 and 4). (I) manipulation of a mug. Upon inflation, the lightweight arm deforms along a predicted path within a few seconds, passing an obstacle to carry the mug on a platform (supplementary Video 5).

If we approximate this profile as the closed axisymmetric profile before additional curving, that is $r_1^*(s^*) \sim r^*(s^*)$ in Eq.3, the position of the line under orthoradial tension can be readily determined. Searching for the condition when the maximum of u^* vanishes leads to:

$$\frac{1}{1 + \epsilon_\alpha} = \max_{s^* > 0} \left(\frac{r^*(s^*)}{s^*} \right) \quad [4]$$

As an illustration, this value can be directly computed in the limit $R \gg w$, where the section is almost circular and the profile follows $r^* = \frac{1}{\pi} [1 - \cos(\pi s^*)]$. Searching for the maximum of the function r^*/s^* leads to the transcendental equation $\pi s^* \sin(\pi s^*) = 1 - \cos(\pi s^*)$. The numerical solution gives $s_{tens}^* \simeq 0.74$ and consequently $\epsilon_\alpha \simeq 0.38$, i.e. $\Delta\alpha_{tens} \simeq 137^\circ$. The curvature varies accordingly from $1/R$ to $(1 + \epsilon_\alpha)/R \simeq 1.38/R$.

In Fig. 4C, we compare the experimental measurement of ϵ_α conducted with polymer sheets with the theoretical predictions from equation (4), and find a very good agreement with

experimental data for $R/w > 2$. The predicted position for the region under tension (red crosses in Fig. 4D) also matches the observed region free from wrinkles. Nevertheless, this region is actually not limited to a line but presents a finite width. We interpret this difference as a consequence of the finite stiffness of the sheet, as described in a seminal paper by King *et al.* (21) in a simpler geometry, and of the simplifying assumption that the profile of the structure is strictly similar to the axisymmetric closed configuration.

Inverse Problem. Having rationalized the change in curvature upon inflation, we propose to use our geometrical model to inverse the problem, i.e. to determine the path of width w leading to an inflated structure of an arbitrary desired 2D shape with free ends. For a given target curve (Fig. 5A & 5E), we first numerically calculate the curvature $\kappa_{tar}(v^*)$, where v^* denotes the curvilinear coordinate along the path to be programmed normalized by the width w (Fig. 5B & 5F). The same parametrization may be used in the flat state since the

inner edge does not stretch nor contract upon inflation and the tube is chosen slender ($\kappa_{tar} \ll 1$). The normalized radius of curvature $R^*(v)$ of the corresponding flat ribbon is then obtained by solving numerically the relationship

$$\frac{1 + \epsilon_\alpha(R^*)}{R^*} = \kappa_{tar} \quad [5]$$

where $\epsilon_\alpha(R^*)$ was computed above and plotted in Fig. 4C (Fig. 5B& 5F). This relationship is rigorously valid only in the case of slowly varying curvatures ($d\kappa_{tar}/dv^* \ll 1$), i.e. when the outline of the path may be locally seen as a path of constant curvature. The contours of the balloons are then plotted with the correct curvature $\kappa(v) = 1/(wR^*(v))$ (Fig. 5C & 5G). If overlap occurs, as in the case of the "Hello" curve, the path is printed in several non overlapping distinct parts, that are bonded together using tape. Upon inflation, we do obtain with great precision the target shape (see Supplementary Videos 3 and 4). Depending on the initial curves, the inflated structures may expand ("Hello") or, conversely contract (waving man). The programming of a simpler and smoother shape, a lemniscate, is shown in Supplementary Fig. S4. This offers a path for a new kind of strong lightweight actuators with programmable shapes. Harnessing geometrical non-linearities, one can predict the complex deformation path to displace objects with mere pressure input. In Fig. 5I and Supplementary Video 5, the octopus-like arm lifts a mug weighting several times its own weight, and carries it to a platform behind an obstacle. Large workload, with particularly large stroke may thus be reached with a very simple object.

Concluding remarks. In this report we have shown that the physics and geometry of apparently mundane flat sealed inflatables such as "mylar balloons" is far richer than expected: the shape of their section includes singularities and a non-trivial distribution of wrinkles; the outline of an inflated curved balloon with free ends overcurves under inflation. Commercially available mylar balloon letters are empirically designed to compensate for this over-curvature. For example the letter "O" has, before inflation, a missing angular sector, and rather looks like a "C" (14) (See supplementary Fig.S3). Our model based on the assumption of perfectly inextensible and infinitely bendable membranes does capture quantitatively this coiling for aspect ratio $R^* > 2$, as well as the shape of the cross sections and the positions of wrinkles. In practical engineering systems, minor corrections due to the finite stiffness of the sheet should nevertheless be accounted for in the case of high pressure (28, 29). Another remaining challenge is to rationalize the mechanical properties of such structures: how does the complex stress pattern revealed by regular folds and wrinkles impact the bending stiffness of the inflated device (22–24)? Beyond this mechanical question, our study remarkably enriches the possibilities for simply manufactured one-dimensional stiff deployable structures for which the inverse problem may be solved.

Materials and Methods

We fabricate the curved balloons by displaying two thin sheets made of the same thermosealable material (TPU (thermoplasticurethane) impregnated nylon fabric, mylar, polypropylene), covered by a sheet

of greaseproof paper, in the working area of an XY-plotter (from Makeblock). A soldering iron with controllable temperature (PU81 from Weller) is then mounted on the tracing head of the plotter (Fig 1A). Using the dedicated software mDraw, we "print" the desired path designed with any vector graphics software. Playing with both temperature and displacement speed of the head, one can simply seal or additionally cut along the path. The envelopes obtained are then connected to the compressed air of the laboratory and inflated. The pressure is then set at typically 0.1 bar, to ensure that we remain in the regime of interest (quasi-inextensible, compression modulus negligible) for our structures with a width on the order of 10 cm, of thickness t of typically $10\mu\text{m}$ and of Young modulus E of the order of the GPa. Cross sections are measured by drawing a radial line on a transparent mylar balloon, a photograph from the side is then taken and the line extracted.

ACKNOWLEDGMENTS. This work has been partially funded by the french ANR SMART. We thank Corrado Maurini for enlightening discussions.

- Rus D, Tolley MT (2015) Design, fabrication and control of soft robots. *Nature* 521(7553):467.
- Shepherd RF, et al. (2011) Multigait soft robot. *Proceedings of the National Academy of Sciences* 108(51):20400–20403.
- Siefert E, Reyssat E, Bico J, Roman B (2019) Bio-inspired pneumatic shape-morphing elastomers. *Nature materials* 18(1):24.
- Deng X (2012) *Clefted equilibrium shapes of superpressure balloon structures*. (California Institute of Technology).
- Wielgosz C, Thomas JC (2002) Deflections of inflatable fabric panels at high pressure. *Thin-walled structures* 40(6):523–536.
- Serruys PW, et al. (1994) A comparison of balloon-expandable-stent implantation with balloon angioplasty in patients with coronary artery disease. *New England Journal of Medicine* 331(8):489–495.
- Jenkins CH (2001) *Gossamer spacecraft: membrane and inflatable structures technology for space applications*. (American Institute of Aeronautics and Astronautics).
- Pagitz M (2007) The future of scientific ballooning. *Philosophical Transactions of the Royal Society of London A: Mathematical, Physical and Engineering Sciences* 365(1861):3003–3017.
- Schenk M, Viquerat A, Seffen K, Guest S (2014) Review of inflatable booms for deployable space structures: packing and rigidization. *Journal of Spacecraft and Rockets* 51(3):762–778.
- Ou J, et al. (2016) aeromorph-heat-sealing inflatable shape-change materials for interaction design in *Proceedings of the 29th Annual Symposium on User Interface Software and Technology*. (ACM), pp. 121–132.
- Paulsen W (1994) What is the shape of a mylar balloon? *The American mathematical monthly* 101(10):953–958.
- Mladenov I, Oprea J (2003) The mylar balloon revisited. *The American Mathematical Monthly* 110(9):761–784.
- Ligaro S, Barsotti R (2008) Equilibrium shapes of inflated inextensible membranes. *International Journal of Solids and Structures* 45(21):5584–5598.
- Pak I (2006) Inflating polyhedral surfaces. *Preprint, Department of Mathematics, MIT*.
- Pak I, Schlenker JM (2010) Profiles of inflated surfaces. *Journal of Nonlinear Mathematical Physics* 17(02):145–157.
- Skouras M, et al. (2014) Designing inflatable structures. *ACM Trans. Graph.* 33(4):63:1–63:10.
- Taylor G (1963) On the shapes of parachutes. *The scientific papers of Sir G I Taylor* 3:26–37.
- Paulsen J, et al. (2015) Optimal wrapping of liquid droplets with ultrathin sheets. *Nature materials* 14(12):1206.
- Kumar D, Paulsen JD, Russell TP, Menon N (2018) Wrapping with a splash: High-speed encapsulation with ultrathin sheets. *Science* 359(6377):775–778.
- Paulsen JD (2019) Wrapping liquids, solids, and gases in thin sheets. *Annual Review of Condensed Matter Physics* 10:431–450.
- King H, Schroll RD, Davidovitch B, Menon N (2012) Elastic sheet on a liquid drop reveals wrinkling and crumpling as distinct symmetry-breaking instabilities. *Proceedings of the National Academy of Sciences* 109(25):9716–9720.
- Vandeparre H, et al. (2011) Wrinkling hierarchy in constrained thin sheets from suspended graphene to curtains. *Physical Review Letters* 106(22):224301.
- Vella D, Ebrahimi H, Vaziri A, Davidovitch B (2015) Wrinkling reveals a new isometry of pressurized elastic shells. *EPL (Europhysics Letters)* 112(2):24007.
- Gérinard JC, Bernal R, Melo F (2004) Wrinkle formations in axi-symmetrically stretched membranes. *The European Physical Journal E* 15(2):117–126.
- Paulsen JD, et al. (2017) Geometry-driven folding of a floating annular sheet. *Physical review letters* 118(4):048004.
- Moulton D, Lessinnes T, Goriely A (2013) Morphoelastic rods. part I: A single growing elastic rod. *Journal of the Mechanics and Physics of Solids* 61(2):398–427.
- Dias M, Dudte L, Mahadevan L, Santangelo C (2012) Geometric mechanics of curved crease origami. *Physical review letters* 109(11):114301.
- Roychowdhury S, DasGupta A (2015) Inflating a flat toroidal membrane. *International Journal of Solids and Structures* 67:182–191.

- 355 29. Roychowdhury S, DasGupta A (2018) Symmetry breaking during inflation of a toroidal mem-
356 brane. *Journal of the Mechanics and Physics of Solids* 121:328–340.

DRAFT



Supplementary Information for

Programming curvilinear paths of flat inflatables

Emmanuel Siéfert, Etienne Reyssat, José Bico, Benoît Roman

Emmanuel Siéfert.

E-mail: emmanuel.siefert@espci.fr

This PDF file includes:

- Supplementary text
- Figs. S1 to S4
- Captions for Movies S1 to S5
- References for SI reference citations

Other supplementary materials for this manuscript include the following:

- Movies S1 to S5

Supporting Information Text

A. Derivation of the equations based on volume maximization. We consider two superposed flat rings, sealed on their edges, of inner radius R and outer radius $R + w$. We assume that when inflated, the membrane is inextensible, but that, being infinitely bendable, it may freely accomodate excess of material with wrinkles. We are interested in the resulting inflated overall shape (and not on the detail of the morphology of the wrinkles). This surface is assumed to remain axisymmetric, with the inextensible meridian always under tension, whereas azimuthal compression could occur on this surface (by forming wrinkles in the actual membrane).

The section of the torus is described by the curvilinear coordinate s along a meridian, the vertical coordinate $z(s)$, the radial coordinate $R + r(s)$, and the angle φ of the tangent to the meridian line with respect to \mathbf{e}_r (Fig S1A). The shape of the section is assumed to be symmetrical with respect to the \mathbf{e}_r axis. In this framework, the equilibrium shape corresponds to the shape which minimizes the energy $U = -pV$, or equivalently, which maximizes the volume V of the toroidal shape obtained by rotational symmetry (1). The volume reads

$$V = 4\pi \int_0^w [R + r(s)] z(s) \cos \varphi \, ds \quad [1]$$

In the radial direction, inextensibility is simply ensured by the limits of the integral, because we assume that meridians are not wrinkled *i.e.* that the membrane is not compressed anywhere in the radial direction. In the azimuthal direction, inextensibility imposes the following inequality

$$\forall s, P(s) \leq P^0(s), \quad [2]$$

where we have defined the apparent perimeter $P(s) = 2\pi(R + r(s))$ of the circle passing through a point s of the section, and $P^0(s) = 2\pi(R + s)$ its initial perimeter. Here this continuous inequality can be greatly simplified in the following way : the radial inextensibility imposes that $\forall s, r'(s) = \cos \varphi \leq 1$, and thus $P'(s) \leq P^{0'}(s)$. Therefore Eq.[2] is satisfied if and only if $P(0) \leq P^0(0)$, or equivalently if and only if $r(0) \leq 0$. An optimal solution must equalize the inequality constraint for at least one curvilinear coordinate, and from the previous equation it must be at $s = 0$. The inextensibility condition [2] thus reduces to the boundary condition:

$$r(0) = 0 \quad [3]$$

Dividing lengths by w , the Lagrangian for the optimization problem may be written in terms of non-dimensional variables and parameters denoted by $*$. We choose here $z(s)$, $r(s)$, and $\varphi(s)$ as independent functions for our optimization problem, for the sake of computation simplicity. The problem is now to maximize

$$\int_0^1 [(R^* + r^*) z^* \cos \varphi + A(\cos \varphi - r^{*'}) + B(\sin \varphi - z^{*'})] \, ds^*, \quad [4]$$

where $(')$ stands for derivatives with respect to s^* . A and B are two Lagrange multipliers enforcing the geometrical relations ($r^{*'} = \cos \varphi$; $z^{*'} = \sin \varphi$), that we shall interpret later. Using classical variational methods, we get the following system of equations for the maximization :

$$\begin{cases} A' = -z^* \cos \varphi \\ B' = -(R^* + r^*) \cos \varphi \\ r^{*'} = \cos \varphi \\ z^{*'} = \sin \varphi \\ [A + z^*(R^* + r^*)] \sin \varphi = B \cos \varphi \end{cases} \quad [5]$$

together with the boundary conditions $A(1) = 0$ because $r^*(0) = 0$ is fixed as seen above (equation [3]), whereas $r^*(1)$ is free. We also have the boundary conditions $z^*(0) = z^*(1) = 0$ from symmetry. We do have the four needed boundary conditions to solve the system of four first order ODEs. It is however interesting to show that these equations are equivalent to equations [1,2] of the main article and related boundary conditions.

Differentiating the last equation in the set of equation [5] and using the other relations to simplify, one gets the equation:

$$\frac{d\varphi}{ds} = -\frac{(R + r) \sin \varphi}{B} \quad [6]$$

It can be easily shown by direct differentiation that the quantity $\sin \varphi / B$ is a constant (using again [5] and [6]). Hence equation [6] shows that $d\varphi/ds$ is strictly proportional to $(R + r)$, and we have recovered equation [1] of the main part of the article where the constant $\sin \varphi / B$ corresponds in physical terms to p/C .

The boundary conditions may also be expressed as function of $\varphi(s)$. $z^*(0) = z^*(1) = 0$ simply imposes that $\int_0^1 \sin \varphi \, ds^* = 0$, and the condition $r^*(0) = 0$ inserted in [6] leads to

$$\varphi'(0) = -pR/C$$

Finally, evaluating the last equation in the set of equation [5] at $s^* = 1$, and knowing that $B = C/p \sin \varphi$, $z^*(1) = 0$ and $A(1) = 0$, we obtain that

$$\varphi(1) = -\pi/2.$$

We may also interpret Lagrange parameters A and B that appear in the variational equations by separating an angular sector of the system with an imaginary cylindrical cut of radius $R + r_0$ and considering the force exerted by the portion $r > r_0$ on the part $r < r_0$ (see Supplementary Fig. S1B). A and B are simply the horizontal and vertical projection of this force.

$$B = C/p \sin \varphi, \quad [7]$$

is the vertical projection of the dimensionless membrane tension per unit angular sector. The total dimensionless horizontal force

$$A = C/p \cos \varphi - z^* \quad [8]$$

also includes a contribution of the pressure on the section in addition to the projected membrane tension.

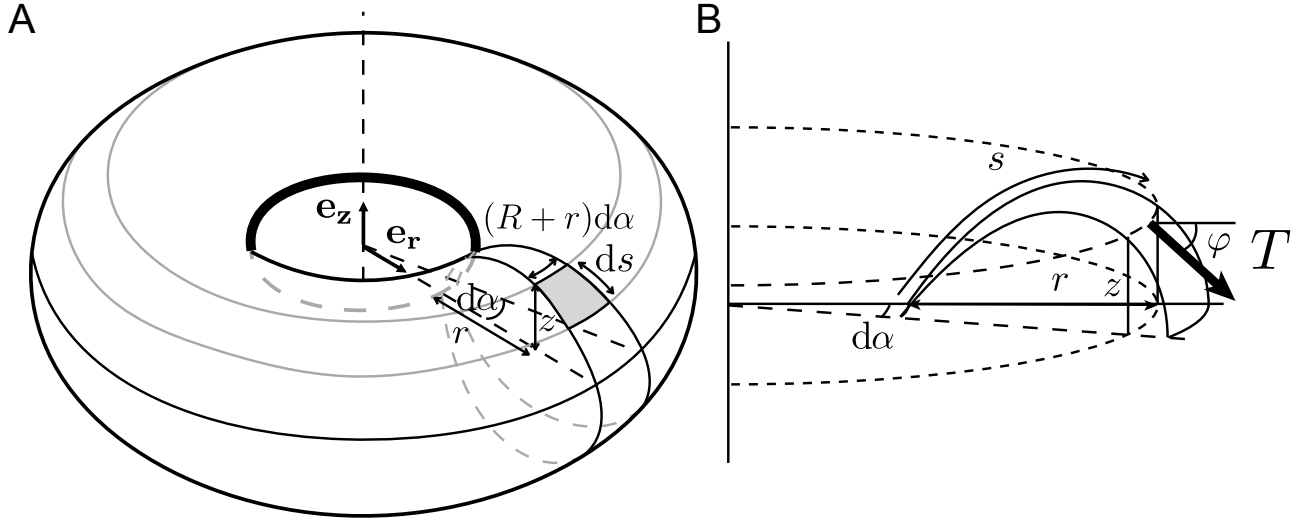


Fig. S1. (A)-(B) Sketch of the inflated toroidal shape with the definition of parameter s , r , z , φ and the tension T . In (B) the intersection between an angular sector $d\alpha$ and a cylinder of radius $R + r$ is shown for the interpretation of the Lagrangian parameters A and B

B. Results interpretation. We can solve this boundary value problem using Matlab function `bvp4c` varying the only non dimensional parameter of the system, the ratio inner over outer radius $R^*/(R^* + 1)$ and compare the results with cross sections measured experimentally (see Fig. 3B in the main manuscript). The theoretical predictions (solid lines) are in remarkable quantitative agreement with the experimental measurements (triangles). For slender rings, that is when $R^*/(R^* + 1) \rightarrow 1$, the cross-section tends to the trivial cross-section of a straight inflated path, a circle. However, when $R^*/(R^* + 1) \rightarrow 0$, the cross-section strongly deviates from a circle and a singularity appears at the inner point $s^* = 0$. One intuitive way to grasp the idea of this shape is the following: the volume of a toroidal shape is the product of the area of the cross section times the length OC from the center of symmetry (O) of the torus to the centroid (C) of the cross-section. When the ring is highly slender, $R^* \gg 1$, the length $OC \in [R^*, R^* + 1]$ is nearly independent of the cross section. The volume optimization reduces thus to the legendary problem of Queen Dido of Carthage, that is, maximizing a surface given a fixed perimeter length, a circle. However, when $R^* \rightarrow 0$ ($OC \in [0, 1]$), the position of the centroid is crucial for the volume optimization problem: the system pays a loss in the area of the cross-section in order to push the centroid away from (O), leading to this asymmetric cross-section shape.

C. Open rings. Inflating such objects with one more degree of freedom, we observe that they remain in-plane, but that the curvature of their outline tends to increase (see Fig.3A of the main text). The open-end condition now allows for an overlapping angle $\Delta\alpha$ to be determined. The previous expression [1] for the volume V is only modified into $(1 + \epsilon_\alpha)V$, where we have noted $\epsilon_\alpha = \Delta\alpha/2\pi$. We may use the modified Lagrangian $(1 + \epsilon_\alpha)L$ in the minimization, and recover the same set of equations [4]. However the perimeters now include overlapping portions of circles with total length $P_{\epsilon_\alpha}(s) = 2\pi(R + (1 + \epsilon_\alpha)r(s))$. The inextensible boundary condition for the inner line now imposes $R_1 = R/(1 + \epsilon_\alpha)$. We see that the value of the strain ϵ_α determines the radius of the curvature of the inner circle and the shape of the section (within the previously calculated family). Finally the free parameter ϵ_α may be determined by maximizing the corresponding volume $V(\epsilon_\alpha)$, provided the sections obey the inextensibility condition (2) for each of their points.

The volume is numerically found to be an increasing function of ϵ_α . The optimal solution is thus expected to have the maximum ϵ_α that satisfies the inextensibility condition (2), which is shown in Fig. 4B of the main document.

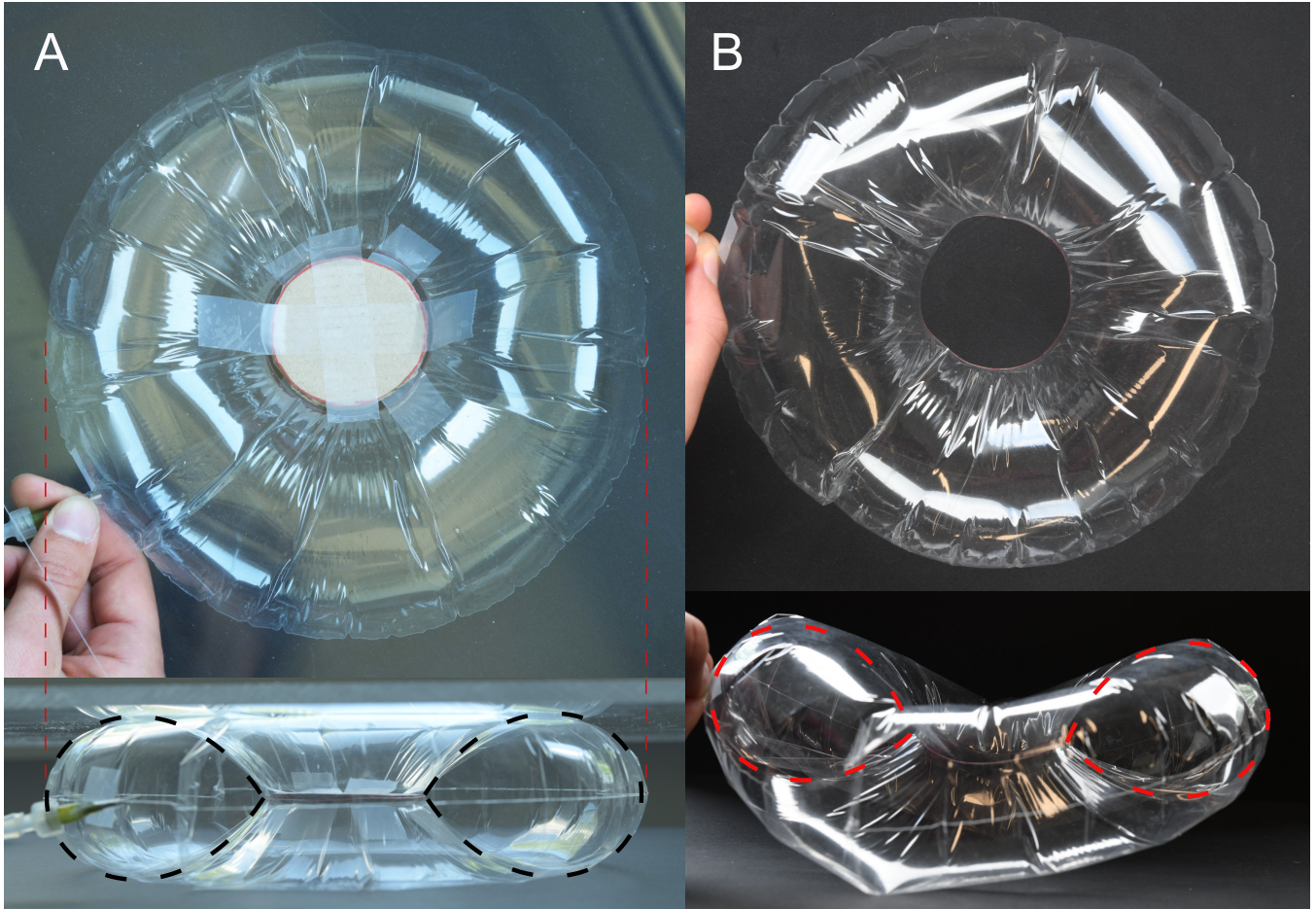


Fig. S2. Pictures of (A) constrained and (B) unconstrained inflated annuli. (A) The toroidal shape is constrained to remain in plane by two parallel plates with a controlled gap. (B) The same object freely buckles out of plane when the constraint is released. However, the cross sections barely evolves and match the theoretical prediction in dashed line.



Fig. S3. Pictures of the same commercial mylar balloon before (left) and after (right) inflation. The letter, which looks like a "C" in the rest state, coils onto an "O" upon inflation.

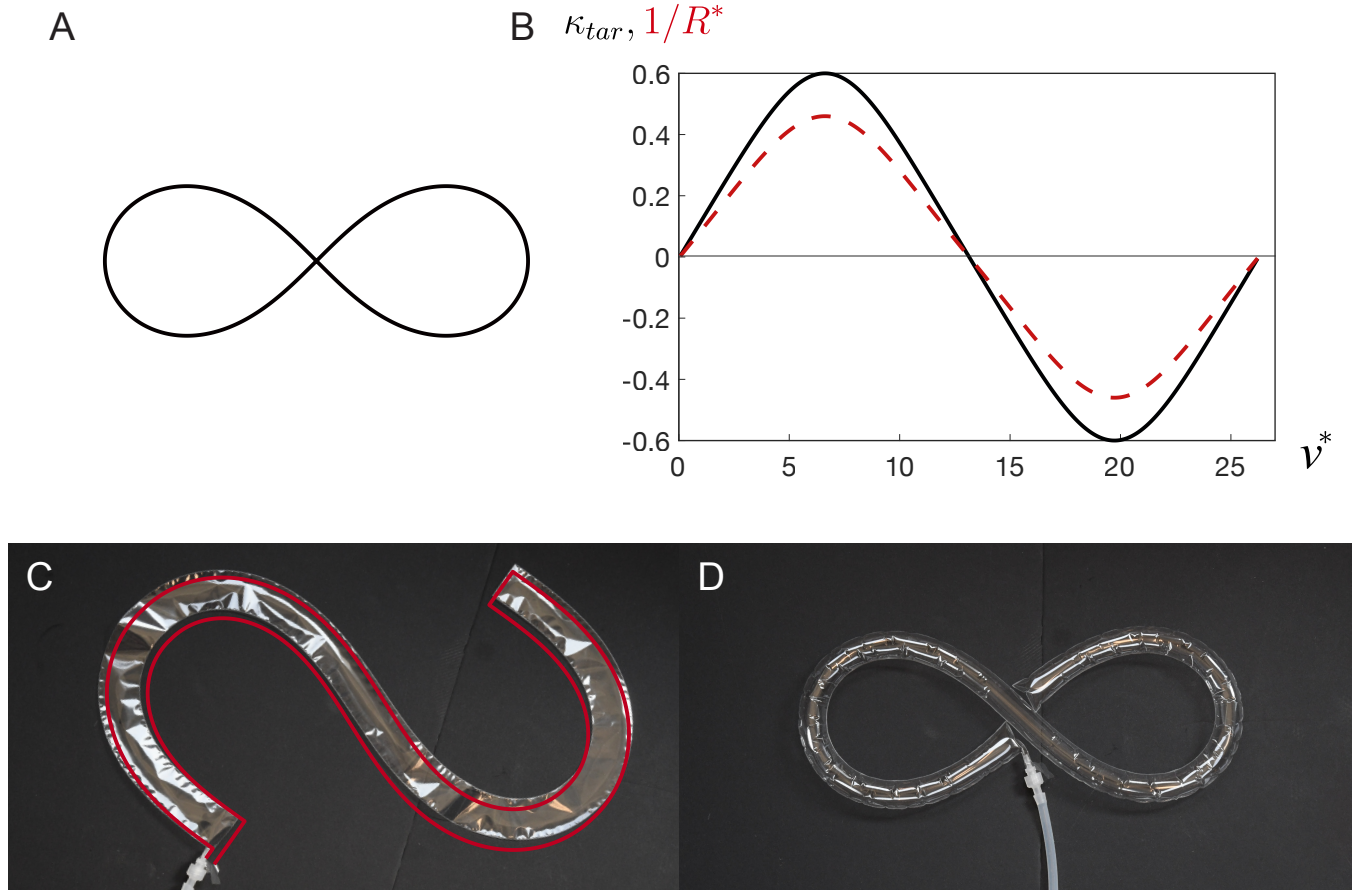


Fig. S4. Programming of a lemniscate. (A) Target outline, (B) normalized curvature of the lemniscate κ_{tar} and of the fabrication state $1/R^*$, computed using equation [5] in the main article. The corresponding pattern on top of a picture of the structure in the flat state is shown in (C). (D) Upon inflation, the structure coils into the target lemniscate outline.

Movie S1. Inflation of a flat closed ring. The inflated structure surprisingly buckles out of plane. The ring (inner radius $R = 85mm$ and width $w = 51mm$) is made of TPU coated Ripstop nylon fabric 20den, from Extremtextil.

Movie S2. Inflation of a flat open ring. The inflated structure overcurves and exhibits an excess angle. The ring (inner radius $R = 60mm$ and width $w = 17mm$) is made of TPU coated Ripstop nylon fabric 20den, from Extremtextil.

Movie S3. Programming of a “waving man”. Upon inflation, the flat sealed path is programmed to shape the contour of a waving man. The structure (of width $w = 1.5mm$) is made of a polypropylene sheet of thickness $t = 16\mu m$.

Movie S4. Programming “hello”. Upon inflation, the flat sealed path is programmed to shape the handwritten “hello”. The structure (of width $w = 1.2mm$) is made of a polypropylene sheet of thickness $t = 16\mu m$.

Movie S5. Manipulation of a mug. Upon inflation, the flat sealed arm deforms along a predicted path, passing an obstacle to carry and drop the mug on a platform. The arm is made of TPU coated nylon fabric 210den from Extremtextil.

References

1. Paulsen W (1994) What is the shape of a mylar balloon? *The American mathematical monthly* 101(10):953–958.